Intensity-resolved measurement of above-threshold ionization of Ar-H_2O

Adrian Platz,[1] Sebastian Hell,[1] Yinyu Zhang,[1] Bo Ying,[1,2] Gerhard G. Paulus,[1,2] and Matthias Kübel[1,2,*]
[1]*Institute for Optics and Quantum Electronics, Universität Jena, D-07743 Jena, Germany*
[2]*Helmholtz Institute Jena, D-07743 Jena, Germany*

(Received 15 May 2023; revised 21 September 2023; accepted 11 October 2023; published 3 November 2023)

Above-threshold ionization (ATI) by femtosecond laser pulses centered at 515 nm is studied for a gas mixture containing the van der Waals complex Ar-H_2O. By detecting photoions and photoelectrons in coincidence, the ATI spectra for Ar, Ar_2, H_2O, and Ar-H_2O are discerned and measured simultaneously. Using an intensity-scanning technique, we observe the red shift of the ATI spectra as a function of the laser intensity. The intensity-dependent shift of the ATI peak positions observed for Ar-H_2O and H_2O match but significantly differ from the ones measured for Ar and Ar_2. This indicates that the photoelectron is emitted from the H_2O site of the complex and the vertical ionization potential of Ar-H_2O is determined as (12.4 ± 0.1)eV. For rescattered electrons, however, an enhancement of high-order ATI is observed for Ar-H_2O, as compared to H_2O, suggesting that the relatively large Ar atom acts as a scattering center, which influences the ionization dynamics.

DOI: 10.1103/PhysRevA.108.053106

I. INTRODUCTION

Rare-gas compounds exhibit rich light-matter interactions and serve as model systems for electron dynamics in weakly bound molecules. A prominent example is interatomic Coulombic decay, which has been first observed in Ne_2 and studied using extreme ultraviolet radiation [1,2]. Also in intense optical fields, rare-gas dimers have attracted significant interest [3–5] but only few studies have explored light-matter interaction in more complex rare-gas compounds [6]. A notable example for such complex target is Ar-H_2O, which has been extensively studied in the past using infrared vibrational spectroscopy [7–11]. One focus of attention has been the location of the energy minimum in the Ar-H_2O intermolecular potential energy surface. After initially contradicting results, studies have converged to the finding that the argon atom resides in the plane of the water molecule, at an angle close to one of the hydrogen atoms but at roughly four times the distance from the oxygen atom [7,9,12,13]. Despite this progress, ionization experiments of Ar-H_2O have been scarce. Consequently, little is known about the structure of the Ar-H_2O cation.

Structural and dynamical information from atoms and molecules has been successfully inferred from above-threshold ionization (ATI) spectra, for example using laser-induced electron diffraction [14–16], or photoelectron momentum imaging [4,17,18]. For recent reviews see Refs. [19,20]. Moreover, spectroscopy of electronic states in polyatomic molecules has been demonstrated in channel-resolved ATI experiments [21,22]. However, accurately measuring the ionization potential using ATI is challenging since the ATI peak positions sensitively depend on the laser intensity. The position of the Sth ATI peak can be described by (atomic units are used if not otherwise stated)

$$E_S = (N + S)\omega - E_{\mathrm{IP}} - \Delta E(I), \tag{1}$$

where ω is the photon energy, E_{IP} is the ionization potential of the target atom or molecule, $N = \lceil E_{\mathrm{IP}}/\omega \rceil$ is the minimum number of photons required to overcome E_{IP}, and $\Delta E(I)$ is an intensity-dependent peak shift. The latter is often approximated by the ponderomotive potential $U_P = \frac{I}{4\omega^2}$, representing the ac Stark shift of the ionization continuum. In addition, the ground state exhibits an intensity-dependent level shift, as well. In the absence of resonances and for not too intense fields, the ac Stark shift can be reasonably well approximated by the dc Stark shift, calculated by second-order perturbation theory [23]. It is given in terms of the peak intensity $I = \mathcal{E}_0^2$, where $\mathcal{E}_0$ is the peak value of the electric field, and the ground-state polarizability α of the respective atom or molecule, by

$$\delta E = -\alpha I/4, \tag{2}$$

and is usually negative. Hence, the ground-state Stark shift usually increases the peak shift $\Delta E(I)$. Note that this does not hold in the presence of resonances. For example, Nicklich *et al.* observed an intensity-dependent blue shift in the multiphoton ionization of Cs by visible wavelengths [24]. The intensity-dependent peak shift of ATI has been observed in various experiments, which aimed at reducing the focal volume averaging effect [25–27], or identifying the role of resonances [27,28]. In many of these experiments, the Stark shift of the ground state has been neglected.

Here, we present intensity-resolved measurements of ATI of Ar, Ar_2, H_2O, and Ar-H_2O by 515 nm femtosecond laser pulses. The data allows us to extract the unknown ionization potential of Ar-H_2O and infer that the electron is emitted from the H_2O site of the compound. In contrast to this, we show that elastic electron rescattering also occurs on the argon atom, whose presence significantly enhances the elastic scattering cross section of Ar-H_2O with respect to H_2O.

*matthias.kuebel@uni-jena.de

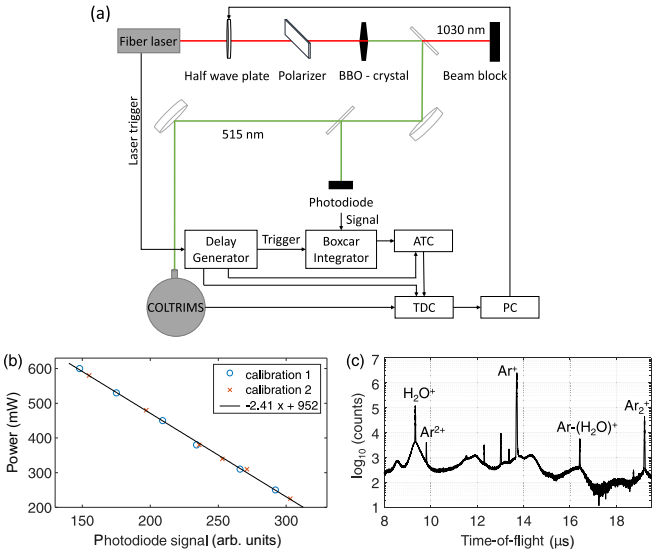

FIG. 1. (a) Schematic of the experiment for intensity-resolved coincidence measurements of above-threshold ionization. The power of the femtosecond laser pulses at 1030 nm is controlled using a motorized half-wave plate followed by a polarizer. The laser frequency is doubled in a BBO, and the two colors are separated. The laser power at 515 nm is measured by a photodiode and a boxcar integrator. In the data acquisition computer, the measured laser power is correlated with the ion and electron momenta detected in the COLTRIMS. (b) Recorded photodiode signal as a function of the laser power, as measured with a power meter before (calibration 1) and after (calibration 2) conducting the main experiment. (c) Ion time-of-flight spectra recorded in the COLTRIMS, with various ionic species marked.

II. EXPERIMENTAL APPROACH

In our experiment, the gas sample containing Ar-H_2O is obtained by bubbling argon at a pressure of 3 bar through water and coexpanding the mixture through a 30-μm nozzle into a high-vacuum vessel. The nozzle was heated to 50°C to avoid clogging by condensed water. The gas jet subsequently passes a 150-μm skimmer and two 1-mm apertures for differential pumping before it enters a cold target recoil ion momentum spectrometer (COLTRIMS), where it intersects the laser focus at a total distance of ≈1.5 m behind the nozzle.

Figure 1(a) shows a schematic of the experiment. Femtosecond laser pulses centered at 1030 nm are obtained from a commercial Yb-doped fiber laser (Active Fiber Systems) operated at 50 kHz repetition rate. The pulses are compressed to 36 fs using an argon-filled hollow-core fiber and suitable chirped mirrors. The laser power is controlled using a motorized half-wave plate and a broadband thin-film polarizer. The transmitted light is frequency doubled using a 300-μm thick beta barium borate (BBO) crystal and the fundamental infrared beam is subsequently discarded. A small fraction of the visible beam is reflected off a wedge and impinges on a photodiode, operated well below saturation. The photodiode signal is further processed using a boxcar integrator to yield a measurement of the pulse energy. Importantly, the photodiode signal is proportional to the laser power recorded with a power meter, as specifically shown for the range of 200–600 mW in Fig. 1(b). Since the second harmonic generation was operated well below saturation, we assume that the pulse duration and beam profiles remains unchanged when the laser power is varied using the motorized half-wave plate. Thus, the photodiode signal is proportional to the intensity in the laser focus. The main beam is focused (7.5 cm focal length) into the center of the COLTRIMS [29] where it intersects the cold gas jet containing the argon-water gas mixture. The momenta of ions and electrons produced in the laser focus are measured in coincidence using time- and position-sensitive detectors on either side of the COLTRIMS. Figure 1(c) shows the ion time-of-flight spectrum, which permits the distinction of various ionic species by their time of flight, and the accurate measurement of the recoil momentum along the laser polarization. Momentum conservation between ion and photoelectron allows us to reliably assign photoelectrons to the ion of the species from which they originate. A total of 6.4×10^4 counts are detected for the Ar-$H_2O^+ + e^-$ and 3.2×10^7 counts for the $Ar^+ + e^-$ coincidence channels.

Besides ion-electron coincidences, coincident events of two ionic species, notably, $Ar^+ + H_2O^+$ Coulomb explosion events are observed. The kinetic energy release of this breakup channel has a mean value of 3.820 eV and a width (standard deviation) of 0.23 eV. Assuming instantaneous double ionization and subsequent propagation of a $1/r$ repulsive potential, this corresponds to a bond distance between Ar and H_2O of (3.77 ± 0.23) Å, in reasonable agreement with but slightly longer than the predicted values of 3.636 Å [7] or 3.603 Å [9]. The experimental result might be systematically shifted towards larger values due to the nonlinear ionization rate, especially in the second ionization step, for which the ionization potential is expected to strongly decrease with increasing internuclear distance. Moreover, we note that the measured KER results from the effective distance of the two charges rather than the center-of-mass distance between Ar and H_2O.

III. RESULTS AND DISCUSSION

A. Intensity-dependent ATI spectra

Figure 2 shows photoelectron energy spectra for ATI of Ar, H_2O, and Ar-H_2O. The spectra exhibit a typical shape with a rapid drop over the first few ATI orders, followed by the rescattering plateau [30] that cuts off around 30 eV (20 eV) for the top (bottom) curve. Remarkably, the signal in the plateau region is approximately two times higher for Ar and Ar-H_2O than for H_2O. We will return to this observation in the context of the photoelectron momentum distributions presented in Fig. 5 below. The photoelectron spectra are modulated by the ATI peaks, which are spaced by the photon energy of 2.4 eV, as expected from Eq. (1). Furthermore, the ATI combs recorded for different targets are shifted with respect to each other, due to the difference in the ionization potentials. A double-peak structure is observed for Ar at higher intensity, which reduces the contrast between ATI peaks and suggests the involvement of resonances. Comparing the ATI combs recorded at higher intensity (top curves) to the ones recorded at lower intensity (bottom curves) reveals the intensity-dependent peak shift. Importantly, a close

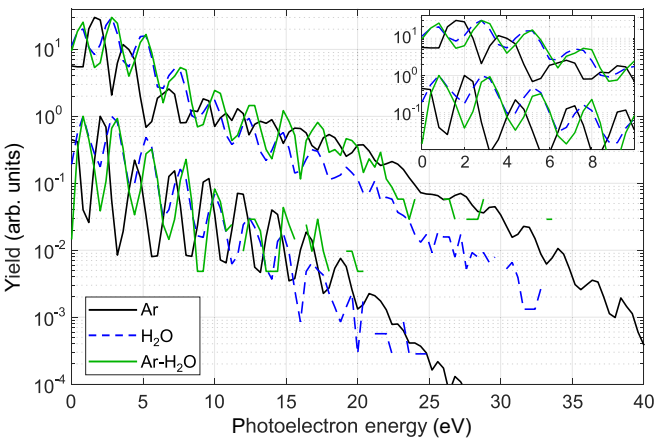

FIG. 2. Measured energy distributions of photoelectrons detected in coincidence with Ar^+ (black), H_2O^+ (dashed blue), and Ar-H_2O^+ (green). Each curve is normalized to its maximum (851059 counts for Ar, 22822 for H_2O, and 1036 for Ar-H_2O). Missing data points are due to a lack of statistics. The top curves represent all data acquired in the experiment with a peak intensity of $\approx 1.0 \times 10^{14}$ W/cm^2, the bottom ones were recorded at $\approx 0.5 \times 10^{14}$W/cm^2. The data sets with different intensity values are vertically displaced for visual convenience. The inset shows the low-energy range of the ATI spectra.

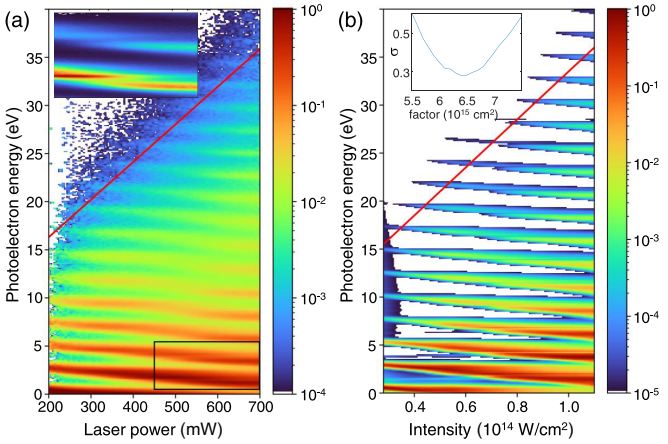

FIG. 3. Intensity-dependent ATI spectra for ionization of Ar by 515 nm light. (a) Experimental results obtained by integrating the measured photoelectron momentum distributions over the full solid angle. The red solid line indicates the cutoff energy of the photoelectron spectra and is described by the expression 0.0391 eV/mW + 8.5 eV. (b) Numerical results obtained by solving the one-dimensional TDSE. The red line is described by the expression 25.0 eV/(10^{14} W/cm^2) + 8.5 eV indicating the high-energy cutoff. The inset shows the standard deviation σ as a function of the proportionality constant between peak intensity and laser power.

examination of the peak positions (see inset of Fig. 2) shows that the offset between the peak positions observed for Ar and Ar-H_2O differ for the two intensity values. Hence, the ionization potential of Ar-H_2O cannot be retrieved simply by comparing the respective ATI peak positions to the ones measured for Ar. The ATI peaks measured for H_2O and Ar-H_2O, however, are close to each other for both intensity values. Whether the offset between the ATI peaks for the two targets allow us to extract the ionization potential of Ar-H_2O will be tested using an intensity scan.

The intensity scan is carried out by scanning the half-wave plate while the laser power transmitted through the polarizer and converted to the second harmonic frequency is tracked by the photodiode, as described above. The measured power-dependent ATI spectra for Ar are presented in Fig. 3(a). The ATI spectra exhibit a pronounced intensity dependence: while the cutoff energy increases proportionally to the laser power, the individual ATI peaks are red shifted and also broadened. This behavior is an impressive manifestation of the focal volume effect: with increasing peak intensity, more and more intensity values contribute to the ATI yield. Since different intensity values correspond to different peak positions, the peaks in the observed ATI spectra are broadened and eventually washed out. In addition, Freeman (multiphoton) resonances [31,32] lead to horizontal features in the intensity-dependent ATI spectrum (see inset of Fig. 3), and are likely responsible for the double-peak structure observed for Ar in Fig. 2 at higher intensity.

The intensity-resolved ATI spectra allow us to find the proportionality constant between measured laser power and peak intensity. This is achieved by comparison of the experimental results to numerical results displayed in Fig. 3(b). These were obtained by solving the one-dimensional time-dependent Schrödinger equation (TDSE) using the split-operator method. The Hamiltonian is given by $H(x,t) = \frac{Z}{|x|+\alpha} + \mathcal{E}(t) \cdot x$. The soft-core parameters Z and α were tuned such that the energies of the ground state and first-excited state of the model atom match those of real argon. The laser field $\mathcal{E}(t) = \mathcal{E}_0(t) \cos \omega t$ has a Gaussian pulse envelope $\mathcal{E}_0(t)$ with a full width at half-maximum of 40 fs and a carrier frequency of $\omega = 0.088$ a.u. The calculated photoelectron spectra were integrated over a Gaussian focal volume [33] and agree well with the measured ones. The proportionality constant between peak intensity and laser power in the experimental data is determined by minimizing the standard deviation between the positions of ATI peaks of orders 1–10 in the measured and calculated ATI spectra. We find best agreement for $(6.40 \pm 0.30)\frac{\text{mW}}{\text{TW/cm}^2}$. The uncertainty indicates the range in which the standard deviation increases by no more than 10%, see inset of Fig. 3(b). Using this conversion, we confirm that the high-energy cutoff of the spectra can be adequately described by the extended cutoff law proposed in Ref. [34]: $E_{\text{max}} = 10U_P + 0.538E_{\text{IP}}$, as indicated by the red lines in Fig. 3.

B. Peak shifts and ionization potential of Ar-H_2O

In order to quantitatively analyze the intensity-dependent ATI spectra for all targets, we extract the ATI peak positions from the measured photoelectron spectra as follows. The photoelectron energy distribution $Y(E)$ around the first ATI peak is fitted by a Gaussian,

$$Y(E) = A \exp\left(-\frac{(E - E_C)^2}{\text{w}^2}\right) + Y_0. \tag{3}$$

We note that, especially for high intensities, the shape of the ATI peaks deviates significantly from a Gaussian shape.

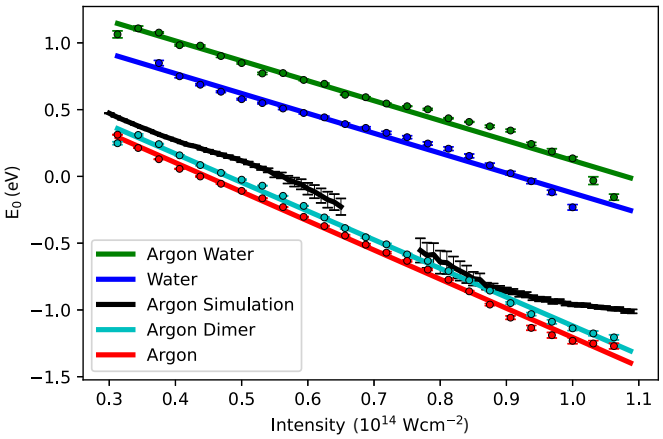

FIG. 4. Intensity-dependent ATI peak positions for various targets. Shown is the measured offset energy of the ATI comb for Ar, Ar_2, H_2O, and Ar-H_2O, as function of the peak intensity. The colored solid lines represent linear fit functions to the data. The peak positions extracted for the simulated data is also shown (black). Around 7×10^{13} W/cm^2, no accurate fit could be obtained due to strong modulations in the calculated photoelectron spectra.

Nevertheless, we obtain good agreement for the peak positions, see Fig. 6, which shows the measured intensity-dependent spectra along with the retrieved centroids of the ATI peaks measured at each laser power and target. The procedure is repeated for 25 different values of the measured laser power, which yields the intensity dependence of the ATI peak positions displayed in Fig. 4.

Figure 4 shows the offsets $E_0 = E_C - 2.4$eV of the ATI comb, retrieved by the fitting procedure described above, as a function of the calibrated laser intensity. Indeed, the ATI peaks measured for Ar and Ar-H_2O exhibit significantly different shifts as a function of intensity. In contrast, the intensity dependence of the ATI peak positions measured for Ar and Ar_2 are nearly identical. Indeed, the ionization potentials of Ar (15.76 eV) and Ar_2 (15.65 eV) are very close and their ATI peaks exhibit only a small offset with a mean of (0.08 ± 0.01) eV, in good agreement with the difference in ionization potential. Analogously, the energy offset between the ATI peaks measured for H_2O and Ar-H_2O remains essentially constant at 0.26 eV within a margin of ± 0.06 eV over the entire intensity range studied in the present experiment. Therefore, it is reasonable to assume that the peak offset corresponds to the difference in ionization potential [cf. Eq, (1)]. With the known ionization potential of H_2O of 12.6 eV, we find a value of (12.4 ± 0.1) eV for Ar-H_2O, where the uncertainty corresponds to the statistical error of the differences in the measured peak positions. We point out that this deviation is independent of the intensity determination conducted above.

We will now further investigate the differences in the intensity dependence of the ATI peak positions recorded for different species. Clearly, the red-shift of the ATI peaks [cf. Eq. (1)] is target dependent. Specifically, the linear fit functions, applied over the entire intensity range of the experiment, yield a slope of $-2.2\,\text{eV}/(10^{14}\,\text{W/cm}^2)$ for Ar and Ar_2. These values are in reasonable agreement with the ponderomotive shift of $-2.5\,\text{eV}/(10^{14}\,\text{W/cm}^2)$ for 515-nm light and the difference is consistent with the effect of focal volume averaging. The TDSE results for Ar exhibits some deviations from linearity, likely due to the effect of resonances. Up to an intensity of approximately 1.0×10^{14}W/cm^2, the intensity-dependent peak shift of the TDSE results agrees with the experimental results, however, the curve is blue shifted by approximately 0.2 eV. Such deviation is possible despite the intensity calibration because the fitting performed above is carried out for the positions of ATI orders 1–10, while in Fig. 4, only ATI order 1 is analyzed. Above 1.0×10^{14}W/cm^2, the measured and calculated peak positions deviate, potentially because the influence of resonances is exaggerated in the one-dimensional TDSE calculations. This observation emphasizes that the linear relationship between ATI peak position and intensity is only applicable in the absence of resonances.

The ATI peak shift measured for Ar-H_2O and H_2O is only $-1.5\,\text{eV}/(10^{14}\,\text{W/cm}^2)$, significantly less than the ponderomotive shift of $-2.5\,\text{eV}/(10^{14}\,\text{W/cm}^2)$ for 515-nm light. A first candidate to explain the observed differences between Ar and Ar_2 on one hand and H_2O and Ar-H_2O on the other hand is the ac Stark shift of the ground state. However, the ground-state polarizabilities of argon ($\alpha_{\text{Ar}} = 11.07\,\text{a}_0^3$) and water ($\alpha_{\text{H2O}} = 10.74\,\text{a}_0^3$) [35–37] are very similar and both lead to a Stark shift of the ground-state energy by $-0.2\,\text{eV}/10^{14}\,\text{W/cm}^2$. Hence, the difference of ground-state polarizabilities for argon and water is too small to explain the observed difference in the intensity-dependent ATI peak shifts of the two targets. Furthermore, as the different shift is observed over the entire intensity range, resonances are unlikely to be responsible for the observed differences. We propose that the smaller red shift of the ATI peaks observed for H_2O and Ar-H_2O results from the permanent dipole [23]. Its effect may become measurable due to the orientation dependence of the ionization probability of water [38]. However, a quantitative calculation of the intensity-dependent ATI peak shift of water is outside the scope of the present paper.

C. Rescattering from Ar-H_2O

In this section, we return to the observation of enhanced backscattering from Ar-H_2O with respect to H_2O. Figure 5 presents the photoelectron momentum distributions measured for Ar-H_2O (top half), H_2O (bottom left quadrant), and Ar (bottom right quadrant) corresponding to the ATI spectra presented in Fig. 2 at high intensity. The momentum distribution measured for Ar_2 is compared to the one for Ar in Fig. 7. The central, low-energy, part of the momentum distributions for all three targets are governed by direct electron emission and full ATI rings are observed. At energies significantly larger than $2U_P$, corresponding to $p \approx 0.6$ a.u., rescattered electrons dominate and the angular distributions are significantly narrower such that only segments of the ATI rings are observed.

We first compare Ar-H_2O to H_2O and observe that the low-energy part of the momentum distribution is nearly identical for the two targets. The slightly lower ionization potential of Ar-H_2O leads to slightly larger radii of the ATI rings. In the high-energy part along the laser polarization, the signal observed for Ar-H_2O is larger than for H_2O. This is evident for

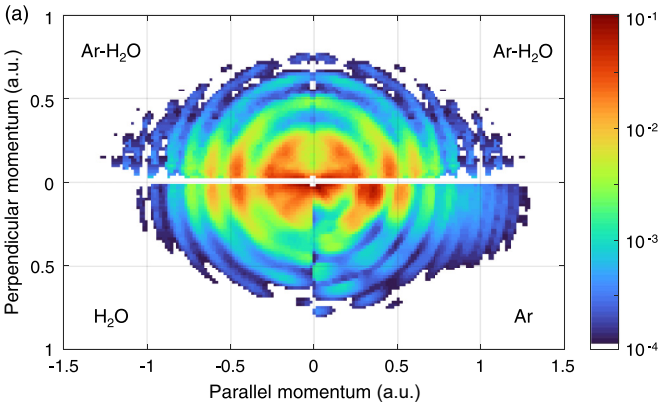

FIG. 5. (a) Photoelectron momentum distribution recorded for nondissociative single ionization of Ar-H_2O (top half), compared to the ones recorded for H_2O (bottom left), and Ar (bottom right). The ionization yield is integrated over all intensity values and normalized to 1 by dividing by the number of detected events for each species. The plot shows the normalized ionization yield per momentum bin, as a function of the momentum components parallel $p_{||} = p_z$ and perpendicular $p_\perp = \sqrt{p_x^2 + p_y^2}$ to the laser polarization, taking into account the appropriate Jacobian. The minimum of the color scale is limited by the low statistics of the Ar-H_2O channel.

the highest ATI peaks but also the signal in the intermediate ones is higher by a factor of ≈2, see Fig. 2. This enhancement suggests a larger contribution from backscattering in the case of Ar-H_2O. Compared to Ar (bottom right quadrant), however, the signal remains somewhat lower. The stronger signal observed for Ar might be a consequence of focal volume averaging, which leads to higher effective intensity for Ar, and therefore higher signal at larger electron momenta. Our results suggest that in Ar-H_2O, the relatively large Ar atom acts as a scattering center, which enhances the contribution of backscattering to the photoelectron yield. Indeed, for the differential elastic electron scattering cross section around 180°, two to three times larger values have been

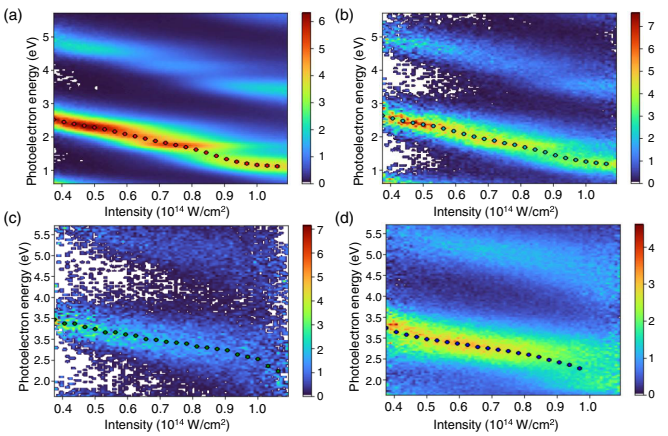

FIG. 6. Intensity-dependent ATI spectra of (a) argon, (b) argon dimer, (c) argon-water, and (d) water. The dots mark the centroids of Gaussians fitted to the experimental data at various intensity values. The statistcal error of the fits is on the order of the dot size.

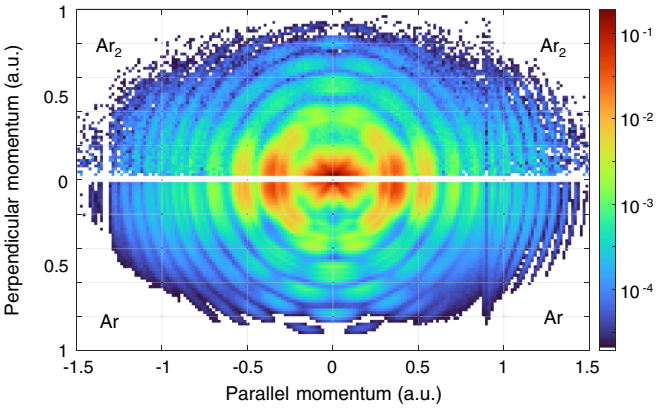

FIG. 7. Same as Fig. 5 but shown is the momentum distribution recorded for nondissociative single ionization of Ar_2 (top half) compared to the one recorded for Ar (bottom half), as in Fig. 5. At $p_{||} \approx -1.3$ a.u. and $p_{||} \approx 0.8$ a.u., the detector provides no resolution for the perpendicular momentum.

reported for Ar [39] than for water [40], consistent with our results.

IV. SUMMARY AND OUTLOOK

In conclusion, we have presented measurements of ATI of Ar-H_2O and compared them to simultaneous measurements of both Ar and H_2O. We found that the peak shift for Ar-H_2O matches that for H_2O, while the ionization potential is lowered by some 0.2 eV with respect to H_2O. These observations indicate that, on the one hand, strong-field ionization occurs on the H_2O side of the weakly bound van der Waals molecule. On the other hand, the reduction of the ionization potential indicates that the molecular ion is more tightly bound than neutral Ar-H_2O. This raises the question about details of the potential energy landscape of the Ar-H_2O cation, for example where the argon atom resides with respect to the H atoms. A suitable tool to shed light on this question is laser-driven Coulomb explosion imaging. While the Ar atom has little effect on the initial step of strong-field ionization, we have further shown that elastic rescattering in Ar-H_2O is enhanced by the presence of the Ar atom. By extension to inelastic rescattering, this suggests the existence of a special mechanism for nonsequential double ionization, where a first electron is emitted from water and its subsequent recollision with the parent ion leads to ionization of the argon atom. This mechanism could lead to a peculiar effect: at relatively low intensity and sufficiently long wavelength, Ar-H_2O could be doubly ionized even before single ionization of Ar becomes efficient.

ACKNOWLEDGMENTS

We thank T. Weber, A. Rose, H. Wöhl, F. Ronneberger, T. Farhadova, J. Yu, S. Voss, and A. Czasch for technical support, in particular when setting up the COLTRIMS. Fruitful discussions with M. Lesiuk and R. Della Picca are acknowledged. This work has been funded by the DFG under Project No. 437321733.

APPENDIX A: INTENSITY-DEPENDENT ATI PEAK POSITIONS

Figure 6 shows experimental results for the four targets along with the centroids obtained from the fitting procedure described above. The fitting is performed in a range of ±1 eV around the approximate position of the first ATI peak. The accuracy of the results is not notably improved if the fitting is repeated for ATI peaks of higher order. The zeroth ATI peak was ignored because of channel closing. In the case of water, no accurate fit was obtained at the highest intensities used in the experiment.

APPENDIX B: PHOTOELECTRON MOMENTUM DISTRIBUTION FOR ARGON DIMERS

Figure 7 compares the photoelectron momentum distributions recorded for nondissociative single ionization of Ar_2 to that for Ar. The momentum distributions for the two targets are very similar to each other, in agreement with earlier experiments using 800-nm light [41]. A slight yield enhancement at minimal electron energy reported for the dimer in Ref. [41] can be identified.

[1] T. Jahnke, U. Hergenhahn, B. Winter, R. Dörner, U. Frühling, P. V. Demekhin, K. Gokhberg, L. S. Cederbaum, A. Ehresmann, A. Knie, and A. Dreuw, Interatomic and intermolecular coulombic decay, Chem. Rev. **120**, 11295 (2020).

[2] F. Trinter, T. Miteva, M. Weller, A. Hartung, M. Richter, J. B. Williams, A. Gatton, B. Gaire, J. Sartor, A. L. Landers, B. Berry, I. Ben-Itzhak, N. Sisourat, V. Stumpf, K. Gokhberg, R. Dörner, T. Jahnke, and T. Weber, Ultrafast temporal evolution of interatomic Coulombic decay in NeKr dimers, Chem. Sci. **13**, 1789 (2022).

[3] C. Wunderlich, E. Kobler, H. Figger, and T. W. Hänsch, Light-induced molecular potentials, Phys. Rev. Lett. **78**, 2333 (1997).

[4] M. Kunitski, N. Eicke, P. Huber, J. Köhler, S. Zeller, J. Voigtsberger, N. Schlott, K. Henrichs, H. Sann, F. Trinter, L. Ph. H. Schmidt, A. Kalinin, M. S. Schöffler, T. Jahnke, M. Lein, and R. Dörner, Double-slit photoelectron interference in strong-field ionization of the neon dimer, Nature Commun. **10**, 1 (2019).

[5] J. Tong, X. Liu, W. Dong, W. Jiang, M. Zhu, Y. Xu, Z. Zuo, P. Lu, X. Gong, X. Song, W. Yang, and J. Wu, Probing resonant photoionization time delay by self-referenced molecular attoclock, Phys. Rev. Lett. **129**, 173201 (2022).

[6] J. Wu, M. Kunitski, L. P. H. Schmidt, T. Jahnke, and R. Dörner, Structures of N_2Ar, O_2Ar, and O_2Xe dimers studied by Coulomb explosion imaging, J. Chem. Phys. **137**, 104308 (2012).

[7] R. C. Cohen and R. J. Saykally, Determination of an improved intermolecular global potential energy surface for Ar–H_2O from vibration–rotation–tunneling spectroscopy, J. Chem. Phys. **98**, 6007 (1993).

[8] T. C. Germann and H. S. Gutowsky, Nuclear hyperfine interactions and dynamic state of H_2O in Ar–H_2O, J. Chem. Phys. **98**, 5235 (1993).

[9] F. Tao and W. Klemperer, Accurate *ab initio* potential energy surfaces of Ar–HF, Ar–H_2O, and Ar–NH_3, J. Chem. Phys. **101**, 1129 (1994).

[10] M. J. Weida and D. J. Nesbitt, High resolution mid-infrared spectroscopy of ArH_2O: The V_2 bend region of H_2O, J. Chem. Phys. **106**, 3078 (1997).

[11] X. Liu and Y. Xu, New rovibrational bands of the Ar–H_2O complex at the ν_2 bend region of H_2O, J. Mol. Spectrosc. **301**, 1 (2014).

[12] J. Makarewicz, *Ab initio* intermolecular potential energy surfaces of the water-rare gas atom complexes, J. Chem. Phys. **129**, 184310 (2008).

[13] D. Hou, Y.-T. Ma, X.-L. Zhang, and H. Li, The origins of intra- and inter-molecular vibrational couplings: A case study of H_2O-Ar on full and reduced-dimensional potential energy surface, J. Chem. Phys. **144**, 014301 (2016).

[14] M. Meckel, D. Comtois, D. Zeidler, A. Staudte, D. Pavicic, H. C. Bandulet, H. Pépin, J. C. Kieffer, R. Dörner, D. M. Villeneuve, and P. B. Corkum, Laser-induced electron tunneling and diffraction, Science **320**, 1478 (2008).

[15] C. I. Blaga, J. Xu, A. D. Dichiara, E. Sistrunk, K. Zhang, P. Agostini, T. A. Miller, L. F. Dimauro, and C. D. Lin, Imaging ultrafast molecular dynamics with laser-induced electron diffraction, Nature (London) **483**, 194 (2012).

[16] B. Wolter, M. G. Pullen, A. T. Le, M. Baudisch, K. Doblhoff-Dier, A. Senftleben, M. Hemmer, C. D. Schröter, J. Ullrich, T. Pfeifer, R. Moshammer, S. Gräfe, O. Vendrell, C. D. Lin, and J. Biegert, Ultrafast electron diffraction imaging of bond breaking in di-ionized acetylene, Science **354**, 308 (2016).

[17] S. Eckart, M. Kunitski, M. Richter, A. Hartung, J. Rist, F. Trinter, K. Fehre, N. Schlott, K. Henrichs, L. Ph. H. Schmidt, T. Jahnke, M. Schöffler, K. Liu, I. Barth, J. Kaushal, F. Morales, M. Ivanov, O. Smirnova, and R. Dörner, Ultrafast preparation and detection of ring currents in single atoms, Nature Phys. **14**, 701 (2018).

[18] M. Kübel, Z. Dube, A. Y. Naumov, D. M. Villeneuve, P. B. Corkum, and A. Staudte, Spatiotemporal imaging of valence electron motion, Nature Commun. **10**, 1042 (2019).

[19] U. De Giovannini, J. Küpper, and A. Trabattoni, New perspectives in time-resolved laser-induced electron diffraction, J. Phys. B **56**, 054002 (2023).

[20] K. Amini, A. Chacón, S. Eckart, B. Fetić, and M. Kübel, Quantum interference and imaging using intense laser fields, Eur. Phys. J. D **75**, 275 (2021).

[21] A. E. Boguslavskiy, J. Mikosch, A. Gijsbertsen, M. Spanner, S. Patchkovskii, N. Gador, M. Vrakking, and A. Stolow, The multielectron ionization dynamics underlying attosecond strong-field spectroscopies, Science **335**, 1336 (2012).

[22] J. Mikosch, A. E. Boguslavskiy, I. Wilkinson, M. Spanner, S. Patchkovskii, and A. Stolow, Channel- and angle-resolved above threshold ionization in the molecular frame, Phys. Rev. Lett. **110**, 023004 (2013).

[23] N B Delone and Vladimir P Krainov, AC Stark shift of atomic energy levels, Phys. Usp. **42**, 669 (1999).

[24] W. Nicklich, H. Kumpfmüller, H. Walther, X. Tang, H. Xu, and P. Lambropoulos, Above-threshold ionization of Cesium under femtosecond laser pulses: New substructure due to strongly coupled bound states, Phys. Rev. Lett. **69**, 3455 (1992).

[25] M. A. Walker, P. Hansch, and L. D. Van Woerkom, Intensity-resolved multiphoton ionization: Circumventing spatial averaging, Phys. Rev. A **57**, R701 (1998).

[26] N. A. Hart, J. Strohaber, G. Kaya, N. Kaya, A. A. Kolomenskii, and H. A. Schuessler, Intensity-resolved above-threshold ionization of xenon with short laser pulses, Phys. Rev. A **89**, 053414 (2014).

[27] J. Wiese, J.-F. Olivieri, A. Trabattoni, S. Trippel, and J. Küpper, Strong-field photoelectron momentum imaging of OCS at finely resolved incident intensities, New J. Phys. **21**, 083011 (2019).

[28] C. Wang, Y. Tian, S. Luo, W. G. Roeterdink, Y. Yang, D. Ding, M. Okunishi, G. Prümper, K. Shimada, K. Ueda, and R. Zhu, Resonance-like enhancement in high-order above-threshold ionization of formic acid, Phys. Rev. A **90**, 023405 (2014).

[29] J. Ullrich, R. Moshammer, A. Dorn, R. Dörner, L. P. H. Schmidt, and H. Schmidt-B cking, Recoil-ion and electron momentum spectroscopy: Reaction-microscopes, Rep. Prog. Phys. **66**, 1463 (2003).

[30] G. G. Paulus, W. Nicklich, H. L. Xu, P. Lambropoulos, and H. Walther, Plateau in above-threshold ionization spectra, Phys. Rev. Lett. **72**, 2851 (1994).

[31] R. R. Freeman, P. H. Bucksbaum, H. Milchberg, S. Darack, D. Schumacher, and M. E. Geusic, Above-threshold ionization with subpicosecond laser pulses, Phys. Rev. Lett. **59**, 1092 (1987).

[32] E. Cormier, P.-A. Hervieux, R. Wiehle, B. Witzel, and H. Helm, ATI of complex systems: Ar and C60, Eur. Phys. J. D **26**, 83 (2003).

[33] Y. Zhang, D. Zille, D. Hoff, P. Wustelt, D. Würzler, M. Möller, A. M. Sayler, and G. G. Paulus, Observing the importance of the phase-volume effect for few-cycle light-matter interactions, Phys. Rev. Lett. **124**, 133202 (2020).

[34] M. Busuladžić, A. Gazibegovic-Busuladzic, and D. B. Milosevic, High-order above-threshold ionization in a laser field : Influence of the ionization potential on the high-energy cutoff, Laser Phys. **16**, 289 (2006).

[35] X. Ge and D. Lu, Molecular polarizability of water from local dielectric response theory, Phys. Rev. B **96**, 075114 (2017).

[36] C. Gaiser and B. Fellmuth, Polarizability of Helium, Neon, and Argon: New perspectives for Gas metrology, Phys. Rev. Lett. **120**, 123203 (2018).

[37] M. Lesiuk and B. Jeziorski, First-principles calculation of the frequency-dependent dipole polarizability of argon, Phys. Rev. A **107**, 042805 (2023).

[38] R. D. Picca, J. Fiol, P. D. Fainstein, J. P. Hansen, and A. Dubois, Laser pulse ionization of fixed-in-space H_2O, J. Phys. B **45**, 194009 (2012).

[39] K. L. Bell, N. S. Scott, and M. A. Lennon, The scattering of low-energy electrons by argon atoms, J. Phys. B **17**, 4757 (1984).

[40] L. E. Machado, L. Mu-Tao, L. M. Brescansin, M. A. P. Lima, and V. McKoy, Elastic electron scattering by water molecules, J. Phys. B **28**, 467 (1995).

[41] A. von Veltheim, B. Manschwetus, W. Quan, B. Borchers, G. Steinmeyer, H. Rottke, and W. Sandner, Frustrated tunnel ionization of noble gas dimers with Rydberg-electron shakeoff by electron charge oscillation, Phys. Rev. Lett. **110**, 023001 (2013).